THE JOURNAL OF PHYSICAL CHEMISTRY C
A JOURNAL OF THE AMERICAN CHEMICAL SOCIETY

pubs.acs.org/JPCC

Article

Conflicting Role of Inversion of the $LiMn_2O_4$ Spinel on Lithium-Ion Battery Capacity from First-Principles Calculations

Zijing Wan, Yaxin Xu, Guoqing Sun, Dongwei Xu,* and Xiaobing Luo

Cite This: *J. Phys. Chem. C* 2022, 126, 7374−7382

Read Online

ACCESS | Metrics & More | Article Recommendations | Supporting Information

ABSTRACT: The inversion (Li and Mn interchanging sites) of cathode material $LiMn_2O_4$ (LMO) on the battery capacity is studied from the perspective of Jahn−Teller distortion (JTD) and manganese dissolution. The LMO spinel in the orthorhombic structure with anti-ferromagnetic ordering is studied using spin-polarized density functional theory calculations with anisotropic ($U - J$) corrections. The charge orderings and magnetic moments of the orthorhombic LMO spinel at normal, half-inverse, and full-inverse structures are connected with the battery's properties. It is found that the magnetic moments prefer high spin states in all the cases, and the JTD is mainly due to Mn^{3+}. The existence of Mn^{3+} at octahedral and tetrahedral sites in normal and full-inverse LMO spinel, respectively, induces strong JTD that will reduce the battery capacity. In half-inverse LMO spinel, the cubic-like phase with degraded JTD could retard the capacity decay of lithium-ion batteries, while the existence of Mn_A^{2+} at the tetrahedral sites would aggravate the manganese dissolution and exacerbate the capacity decay. In all, inversion in LMO does not always have a negative effect on battery capacity as JTD and Mn^{2+} manganese dissolution compete with each other.

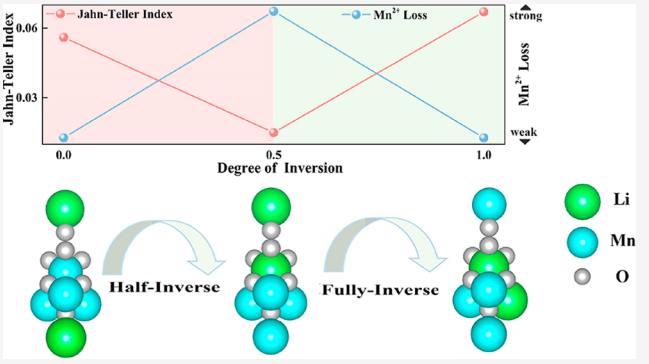

INTRODUCTION

The energy storage capability of lithium-ion batteries is dramatically determined by the cathode material.[1] Up to now, a great deal of effort has been put into developing cathode material with low cost and high energy density. $LiMn_2O_4$ (LMO) is considered as a promising candidate due to its high energy density, high specific power, environmental friendliness, and low cost.[2,3] Furthermore, it is found that LMO has a structural network of three-dimensional channels (along the tetrahedron−octahedron−tetrahedron due to co-planar construction between Li−O tetrahedra and Mn−O octahedra in the LMO spinel), allowing rapid diffusion of small molecules such as lithium ions.[4,5] However, the significant capacity decay of LMO has been a key limitation for its application in lithium-ion batteries. For the stoichiometric LMO, the capacity decay is mainly due to the following two reasons:

(1) Jahn−Teller Distortion (JTD): the distorted tetragonal crystal system is incompatible with the cubic crystal system, which destroys the structural integrity and effective contact between the particles, thus affecting Li^+ diffusion and interparticle conductivity and resulting in capacity loss.[6,7]

(2) Dissolution of Mn: the tracing water in the electrolyte will react with $LiPF_6$ in the electrolyte to form HF, resulting in the disproportionation of LMO as shown in the following equation. Mn^{2+} is dissolved into the electrolyte, and the structure of the spinel is destroyed, leading to the capacity decay of LMO cells.[8,9]

During the continuous charging and discharging of lithium-ion batteries for long periods, the crystal structure is transformed.[10,11] LMO as a CD_2O_4-type bimetallic spinel has a series of cationic arrangements. For example, in the full-inverse spinel, half of the D cations originally at octahedral sites occupy tetrahedral sites (A), and all the C ions originally at tetrahedral sites now occupy the octahedral sites (B).[12,13] This interchange of manganese and lithium-ion positions is called inversion. The degree of inversion X is used to express the proportion of the interchanged positions of lithium ions to the total number of lithium ions. We use Mn_A (Li_A) and Mn_B (Li_B) to stand for the Mn (Li) ions at tetrahedral and octahedral sites separately in this paper.

Received: January 13, 2022
Revised: April 11, 2022
Published: April 22, 2022

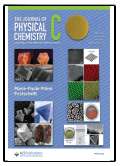

https://doi.org/10.1021/acs.jpcc.2c00274
J. Phys. Chem. C 2022, 126, 7374−7382

Table 1. Summary of the Optimized Lattice Vectors (a, b, c), Atomic Magnetic Moments (m_s), and Free Energy (E_0) of the Normal LMO Spinel for the DFT + U_{eff} and DFT + $(U - J)$ Methods

	U_{eff} = 3.5 eV		U = 4.7 eV		U_{eff} = 5.0 eV		U = 6.2 eV	
	J = 0.0 eV		J = 1.2 eV		J = 0.0 eV		J = 1.2 eV	
	FM	AFM	FM	AFM	FM	AFM	FM	AFM
a (Å)	8.21	8.17	8.20	8.15	8.25	8.21	8.21	8.18
b (Å)	8.20	8.21	8.20	8.18	8.24	8.25	8.20	8.21
c (Å)	8.78	8.74	8.72	8.75	8.77	8.75	8.77	8.75
m_s of Mn^{3+} (μ_B atom^{-1})	3.88	3.81	3.79	3.73	3.98	3.92	3.88	3.82
m_s of Mn^{4+} (μ_B atom^{-1})	3.19	3.15	3.00	2.91	3.36	3.33	3.08	3.04
E_0 (eV)	−387.98	−387.90	−390.88	−391.52	−375.76	−375.59	−378.82	−378.82

$$Li_{1-y}Mn_2O_4 + 2(1-y)HF \rightarrow (3+y)/4Mn_2O_4 + (1-y)LiF + (1-y)H_2O + (1-y)/2MnF_2 \quad (1)$$

How the inversion affects the performance of lithium-ion batteries is unknown. The majority of earlier research on an inverse spinel structure has focused on the structure and electronic properties.[14−16] For example, density functional theory (DFT) simulations of $CoFe_2O_4$ suggested that with the degree of inversion increasing, the band gap of inverse spinel narrows and the electrical conductivity enhances, while the electron transferability of the first step of oxygen reduction gradually becomes weaker. Karim et al. found that under-coordinated Mn cations at surface exchange sites with the fully-coordinated subsurface Li atoms in LMO, effectively reconstructing the (111) surface.[17] Further computational studies[18] considered inversion of the cubic phase LMO spinel with ferromagnetic (FM) ordering, revealing that the Mn atoms experience charge segregation upon spinel inversion. Above 290 K, the LMO crystals are cubic crystal systems with a random distribution of Mn^{3+} and Mn^{4+} cations.[19] When the temperature decreases below 290 K, the Mn^{3+} and Mn^{4+} cation distributions are ordered and the LMO crystal changes from a cubic crystal system to an orthorhombic crystal system with a phase transition.[20,21] However, the inversion of orthorhombic phase LMO has not been studied.

The magnetic characteristics of LMO have been thoroughly documented in the literature,[17,22−27] providing a foundation for simulating various arrangements of LMO with magnetic moments of Mn atoms. As reported in the literature, FM and anti-ferromagnetic (AFM) [110] [↑↑↓↓] magnetic arrangements both exist in the LMO spinel.[17] The [↑↑↓↓] magnetic configuration along the [110] direction[22] is proved by experimental studies combined with X-ray diffraction, neutron diffraction, and sensitivity measurements. In simulations, Zhang et al.[28] calculated eight different AFM magnetic configurations and showed that the ground state is the one with AFM Mn^{3+} layers and FM Mn^{4+} layers alternating along the [001] direction. Ouyang et al.[23] and Karim et al.[17] reported that LMO is in its lowest energy state when Mn atoms in the orthogonal phase spinel are AFM [↑↑↓↓] along the [110] direction, in accordance with experimental observations of low-temperature magnetic arrangements for LMO.[22] In addition, DFT + U calculations for LMO with single-layer graphene using the AFM arrangements along the [110] direction have elucidated the mechanisms of the single-layer graphene modification in the mitigation of Mn loss.[24] Following Scivetti's previous work,[25] Mn^{4+}, Mn^{3+}, and Mn^{2+} sites after inversion are identified on the basis of the computed magnetic moments. It is found that the range of magnetic moments of Mn^{4+}, Mn^{3+}, and Mn^{2+} in simulations are 2.98−3.50 μ_B, 3.77−4.03 μ_B, and 4.55−4.60 μ_B, respectively. For simplicity, the previous work studying the inversion of cubic LMO[18] considered FM magnetic ordering only. The initial AFM ordering will increase the uncertainty of the magnetic momentum arrangement after inversion, which will also be discussed in our study.

In this work, we investigate how the degree of inversion affects battery capacity of the lithium-ion cell whose cathode material is the orthogonal phase LMO spinel with AFM magnetic ordering using DFT + U simulations from the aspects of JTD and manganese valence states of LMO. In addition, we draw the projected density of states (PDOSs) of Mn to help analyze the spin polarization and valence states of the manganese ion.

METHODS

Spin-polarized DFT calculations are performed using the Vienna Ab initio Simulation Package (VASP 5.4.4)[29,30] at a plane-wave energy cutoff of 520 eV. Projector augmented wave pseudopotentials are used to model the core electrons[31] with the 2s 2p and 3d 4s electrons treated as valence for Li and Mn, respectively. The generalized gradient approximation (GGA) of Perdew−Burke−Ernzerhof is selected as the exchange correlation functional.[32] Orthogonal phase spinel bulk LMO calculations employ a 4 × 4 × 4 Monkhorst−Pack K-point mesh and Gaussian smearing with a width of 0.05 eV. Geometry optimizations are conducted via the quasi-Newton method. All atoms in the bulk calculations are subject to full ionic relaxation and are converged to an energy tolerance of 0.1 meV and a force criterion of 0.02 eV/Å.[33]

To correctly investigate the properties of transition metal oxides, a Hubbard correction[34] applied to 3d orbitals to improve the description of the electron localization is a good approximation. There are two commonly used effective Hubbard U values for Mn element in the literature: 3.5[15] and 5 eV.[35] In the GGA + U[36,37] calculations, the Hubbard U value for the Mn element is taken in two ways, one is an isotropic (U_{eff}) and the other is anisotropic ($U - J$) Hubbard.[25] To test the U values, We set four independent calculations as listed in Table 1 for normal spinel LMO.

The values of the initial magnetic moments for the Mn atoms are set to be 3.5 μ_B atom^{-1}[23] with AFM magnetic ordering along the [110] (↑↑↓↓) direction and allowed to relax during simulations. When the degree of inversion X is between 0 and 1, there are several simplified crystal structures associated with each degree of inversion. There are a total of 735,471[18] cation distribution configurations when the whole cell is studied without taking symmetry into account. For

https://doi.org/10.1021/acs.jpcc.2c00274
J. Phys. Chem. C 2022, 126, 7374−7382

simplicity, only one of the four primitive rhombohedral cells is studied in this paper, and 15 cation distribution configurations are obtained without considering symmetry. In the main text, we consider one, three, and three crystal structures with degrees of inversion of 0, 0.5, and 1, respectively, and discuss all the possible structures in the Supporting Information. We also calculate the normal spinel structure with the magnetic ordering (denoted as AFM-I) reported to be the lowest energy in Zhang's paper[28] to compare.

RESULTS AND DISCUSSION

Equilibrium Configuration and Structures. LMO adopts an orthorhombic symmetry *Fddd* (no. 70) structure with experimental lattice parameters of a = 8.20 (Å), b = 8.25 (Å), and c = 8.28 (Å).[20] Based on this structure, we established rhombohedral primitive unit cells with degrees of inversion X = 0 (normal spinel), as shown in Figure 1a. Figure 1b gives the

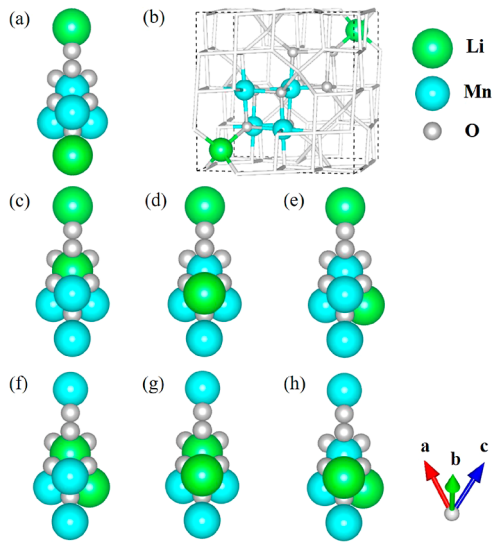

Figure 1. Schematic illustration of the rhombohedral primitive unit cell in the LMO spinel. (a,b) Normal rhombohedral primitive unit cell and the conventional unit cell of a perfect LMO spinel, highlighting one of the four rhombohedral primitive unit cells, (c–e) type I, type II, and type III of the half-inverse rhombohedral primitive unit cell, (f–h) type I, type II, and type III of the full-inverse rhombohedral primitive unit cell.

relative position of the rhombohedral primitive unit cell and the orthorhombic unit structure. Geometry optimization is performed using isotropic (U_{eff}) and anisotropic ($U - J$) Hubbard corrections, respectively. Additional variables, two magnetic orderings (AFM and FM), and two effective Hubbard U values result in eight possible optimization parameters. The lattice parameters, the manganese ion magnetic moments, and the free energy of the system obtained from the eight optimized schemes for the normal spinel LMO are shown in Table 1. The energy of AFM-I magnetic ordering[28] is calculated to be compared after testing the Hubbard correction. The structure with the lowest energy is calculated with the anisotropic Hubbard correction $U - J$ = 3.5 eV and the AFM configuration, which is consistent with the most stable AFM configuration experimentally.[21] The spinel bulk LMO lattice parameters [a = 8.15 (Å), b = 8.18 (Å), c = 8.75 (Å)] obtained from this optimization scheme are in line with Scivetti's[25] simulation results. The anisotropic Hubbard correction $U - J$ = 3.5 eV is then used to test the stability of the structure (AFM-I) proposed by Zhang.[28] The energy of AFM-I ordering is higher than the energy of AFM magnetic ordering along the [110] (↑↑↓↓) direction as the comparison shown in Figure S1 (Supporting Information). We start from the structure with AFM magnetic ordering along [110] (↑↑↓↓) direction to carry out the following study.

From the AFM structure discussed above, we established rhombohedral primitive unit cells with degrees of inversion X = 0.5 and 1, as shown in Figure 1c–h. For X = 0.5, half of the Li ions originally at tetrahedral sites exchange positions with the Mn ions. Figure 1c–e show three typical structures after site interchanging. Furthermore, the other five types for half-inverse rhombohedral primitive unit cells are constructed as shown in Figure S2 (Supporting Information) to verify the consistency of results when exchanging different sites. In addition, we use the orthorhombic unit structure (four times the size of the primitive cell) to test two more possibilities of interchanging lithium ions at tetrahedral sites with Mn ions at octahedral sites for the half-inverse LMO spinel as listed in Table S1 of the Supporting Information. When all lithium ions occupy the octahedral sites, the LMO spinel is full-inverse as shown in Figure 1f–h. The total six types of full-inverse rhombohedral primitive unit cells are displayed in Figure S7 (Supporting Information).

Different from the large c/a ratio of normal LMO in the orthorhombic structure, the structure of LMO at inversion degree X = 0.5 is cubic-like, as can be seen from Table 2 and Table S1 (Supporting Information). When the LMO spinel fully inverses, the structure becomes elongated again with the stretched axis depending on the swapped sites.

Table 2. Summary of the Optimized Lattice Vectors (a, b, c) and Total Energy (E_0) of Bulk LMO with Different Degrees of Inversion

X		a (Å)	b (Å)	c (Å)	E_0 (eV)
0.0		8.15	8.18	8.75	−391.52
0.5	type I	8.33	8.34	8.35	−388.67
	type II	8.33	8.34	8.36	−388.62
	type III	8.35	8.35	8.33	−388.72
1.0	type I	8.11	8.16	8.67	−382.92
	type II	8.20	8.62	8.09	−382.56
	type III	8.64	8.15	8.17	−382.63

Charge and Magnetic Properties. Table 3 and Tables S2 and S4 (Supporting Information) summarize the Bader charge[38] analyzing atomic charges and magnetic moments of LMO with different degrees of inversion. Normally, the Bader charges are systematically underestimated.[15,39] The Bader charges of the monovalent Li_A and Li_B atoms are both about 0.89 e atom^{-1} for all the inversion degrees. For the normal spinel LMO, Mn_B undergoes charge separation. The Bader charges of the positive trivalent and tetravalent manganese ions are 1.71 and 1.87 e atom^{-1} separately. Along the c-axis, Mn_B^{3+} and Mn_B^{4+} are staggered in layers. This charge ordering is different from the lack of charge separation in previous research on the normal spinel of LMO in the cubic structure.[18] For the LMO at inversion degree X = 0.5, the manganese at the octahedral site is tetravalent with the Bader charge of 1.87 e atom^{-1}, and the manganese at tetrahedral site has a much lower Bader charge indicating bivalent manganese. Even though the type IX (interchange of Li and Mn ions mixing

https://doi.org/10.1021/acs.jpcc.2c00274
J. Phys. Chem. C 2022, 126, 7374−7382

Table 3. Atomic Charges (q) and Magnetic Moments (m_s) of the LMO Spinel with Different Degrees of Inversion

		q (e atom^{-1})					m_s (μ_B atom^{-1})					
X		Li_A	Mn_A	Li_B	Mn_B	O	Li_A	Mn_A	Li_B	Mn_B	O	M_s (μ_B u.c^{-1})
0.0		0.89	-	0.00	1.71/1.87	−1.11	0.00	-	0.00	2.91/3.73	0.04	0.00
0.5	type I	0.89	1.49	0.89	1.88	−1.11	0.00	4.49	0.00	2.89	0.01	0.00
	type II	0.90	1.50	0.89	1.88	−1.11	0.00	4.48	0.00	2.89	0.01	0.00
	type III	0.89	1.49	0.89	1.87	−1.11	0.00	4.48	0.00	2.93	0.02	0.00
1.0	type I	-	1.67	0.89	1.81	−1.10	-	3.77	0.00	2.91	0.03	0.00
	type II	-	1.67	0.89	1.88	−1.10	-	3.77	0.00	2.91	0.03	0.00
	type III	-	1.67	0.89	1.80	−1.10	-	3.73	0.00	2.92	0.03	0.00

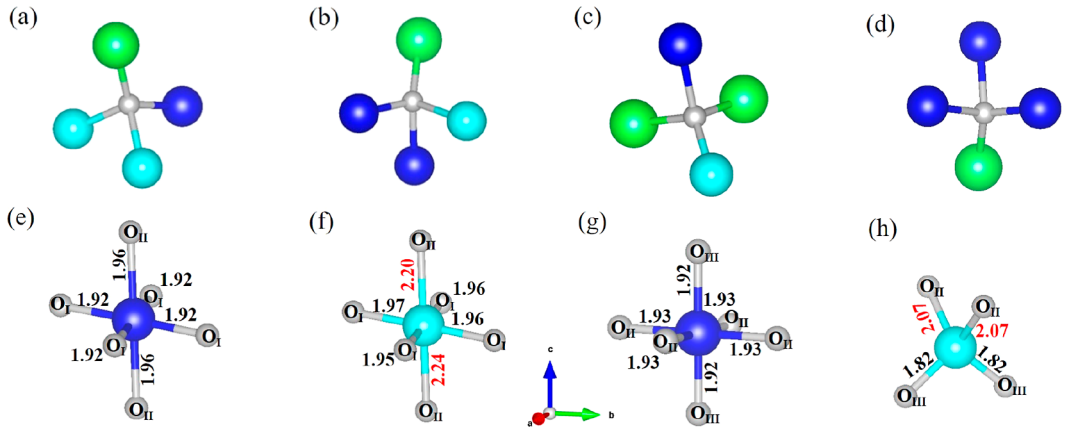

Figure 2. Ball and stick model of the normal and full-inverse spinel LMO. (a−d) local atomic positions around O_I, O_{II}, O_{III}, and O_{IV}, (e,g) non-distorted Mn_B^{4+}−O octahedra in the normal and full-inverse spinel LMO, (f,h) J−T distorted Mn_B^{3+}−O octahedra in the normal spinel LMO, and Mn_A^{3+}−O tetrahedra in the full-inverse spinel LMO. The gray, cyan, blue, and green balls represent O, Mn^{3+}, Mn^{4+}, and Li atoms, respectively.

type I and type III) has the lowest energy, the Bader charge distribution does not change. For the LMO at inversion degree X = 1, Mn_A and Mn_B are positive trivalent and tetravalent, respectively, inferred from the Bader charge listed in Table 3. The charge distribution can also be confirmed by the magnetic moments. As discussed in Scivetti's work,[25] the range of magnetic moments of Mn^{4+}, Mn^{3+}, and Mn^{2+} in simulations are 2.98−3.50 μ_B, 3.77−4.03 μ_B, and 4.55−4.60 μ_B, respectively. At the degree of inversion X = 0, the magnetic moments of Mn_B atoms segregate like the charges: 3.73 μ_B and 2.90 μ_B for the trivalent and tetravalent manganese separately. The magnetic moment of Mn_A^{2+} (Mn_B^{4+}) in spinel LMO with the degree of inversion X = 0.5 is about 4.48 μ_B (2.89 μ_B). The magnetic moment of Mn_A^{3+} in full-inverse spinel LMO is about 3.77 μ_B, in line with Mn_B^{3+} in normal spinel.

The magnetic ordering at different inversion degrees is changing. For normal spinel LMO, the structure with the lowest energy adopts AFM magnetic ordering along the [110] (↑↑↓↓) direction. Half of the Mn_B^{3+} (Mn_B^{4+}) atoms at octahedral sites keep in spin up, and the other half keep in spin down, resulting in a zero net magnetic moment. However, at X = 0.5, there are several exchanging positions of Li and Mn ions (referring to Figure S2 in the Supporting Information), leading to different initial spin polarization arrangements. In the ten possible inverse structures studied in this work, types I, III, IV, and IX have specific magnetic ordering along the [001] direction, types VI, VII, and VIII have magnetic ordering along the [110] direction, and types II, V, and X do not have any magnetic ordering. By comparing the energy of the ten inversion types at X = 0.5, we can conclude that the structures with some sort of magnetic ordering have lower energies and the ones with magnetic ordering along the z-direction are more stable. At X = 1.0, there are six possible inversion types described in Figure S7 (Supporting Information), among which types I, II, III, and V have specific magnetic ordering along the [001] direction, type IV has magnetic ordering along [110], and there is no specific magnetic ordering for type VI. As verified at X = 0.5, the structures with magnetic ordering along the z-direction also have lower energies for full-inverse LMO. It is interesting to note that the specific magnetic ordering does not affect the charge values, magnetic moments (Table 3), and the JTD (discussed later), which are important parameters relating to the performance of the battery. Therefore, we do not consider the specific magnetic ordering after inversion and focus on the normal, type I half-inverse, and type I full-inverse spinel LMO in the following study.

An interesting result for Mn atoms is that the lower the valence, the higher the magnetic moment, which could be understood from the crystal field theory. Since the JTD causes unfrozen orbital angular momentum,[6] according to the crystal field theory, the orbital angular momentum of the manganese atom is partially frozen. The magnetic moments of the manganese ion and the total spin quantum number of Mn have the following relationship

$$M_s = g_l\sqrt{S(S+1)}\,\mu_B \tag{2}$$

where S is the total spin quantum number, which equals half of the unpaired electrons n. For Mn ions, the number of electrons in the 3d shell is less than half full, indicating that the g_l factor is less than two. Then, the magnetic moments can be expressed as follows

$$M_s = (g_l/2)\sqrt{n(n+2)}\,\mu_B \tag{3}$$

https://doi.org/10.1021/acs.jpcc.2c00274
J. Phys. Chem. C 2022, 126, 7374−7382

The outer shell electron configuration of the Mn atom is $3d^5 4s^2$. For Mn^{4+}, Mn^{3+}, and Mn^{2+}, the number of outer shell electrons is 3, 4, and 5, respectively, resulting in increasing magnetic moments. Compared with the previous magnetic moment prediction of different charge values of Mn, the g_l factor is about 1.7. The relationship between charge and magnetic moments also indicates that the electrons remain in the high spin state for all three valence states. It is also worth mentioning that the manganese ion at the tetrahedral site has lower valence and higher magnetic moments compared to the octahedral site, which is related to the local chemical environment.

Jahn−Teller Effect. By further examining the local environment of Mn ions, we find that the change in lattice constants is related to the JTD and the JTD is related to the valence state of Mn ions.

Four types of oxygen ions are defined by the connected neighbor atoms to describe the chemical environment shown in Figure 2a−d. O_I (O_{II}, O_{III}, O_{IV}) connects to two (one, one, and zero) Mn^{3+} ions, one (two, one, and three) Mn^{4+} ion, and one (one, two, and one) Li^+ ion. At $X = 0$, all the Mn ions occupy the octahedral sites with the same chemical environment shown in Figure 2e,f. For the Mn_B^{4+}-O octahedron, the bond length between Mn_B^{4+} and O_I is slightly different from that between Mn_B^{4+} and O_{II}, and there is no obvious bond elongation along any particular direction. However, it is not the case for the Mn_B^{3+}−O octahedron, where a large Mn_B^{3+}−O_{II} bond length indicates strong JTD. Similarly, at $X = 1.0$, the bond lengths between Mn_B^{4+} and O atoms are about the same, at 1.92 and 1.93 (Å) in the Mn_B^{4+}−O octahedron shown in Figures 2g and S8a,b. As for the Mn_A^{3+}−O tetrahedron, there is strong JTD that the bond between Mn_A^{3+} and O_{II} is elongated and a compression is observed for the bond between Mn_A^{3+} and O_{III} in Figures 2h and S8c,d. It is also found in the LMO doped with other ions, such as Fe ions and V ions, that the inversed Mn_A at the tetrahedral site performs similar JTD.[40−42] On examining the local bonding of Mn_A^{2+} (Mn_B^{4+}) with neighboring O ions at the degree of inversion $X = 0.5$, no obvious bond elongation or compression is observed, as shown in Figure S3 and Figure S4 (Supporting Information), indicating that no JTD occurs.

To describe the distribution of transition metal oxides, the distortion index introduced by Baur[43,44] is employed

$$\mathrm{JTI} = \frac{1}{n}\sum_{i=1}^{n}\frac{|l_i - l_{av}|}{l_{av}} \quad (4)$$

where n stands for the number of bonds of transition metal, l_i is the length of bond in different directions, and l_{av} is the average length of all bonds. The JTI of Mn_A^{3+} at the tetrahedral field in the full-inverse LMO spinel and Mn_B^{3+} at the octahedral field in the normal spinel, which both perform strong JTD, is about 0.067 and 0.056, respectively. In contrast, the JTI of Mn_B^{4+} at the non-distorted octahedral field in LMO spinel at $X = 0$, 0.5, and 1 is only about 0.009, 0.015, and 0.002, respectively.

According to the Jahn−Teller theorem, electron configurations with unequal occupancy of degenerate orbitals are not stable, and the JTD could be well understood from crystal field theory. The schematic diagram of the splitting orbital energy levels of Mn_B^{4+}, Mn_B^{3+}, and Mn_A^{2+} is shown in Figure 3. At the tetrahedral field, the Mn_A^{2+} 3d orbitals are split into twofold degenerate e orbitals and threefold degenerate t_2 orbitals. However, Mn_A^{2+} is at the high spin state, and the outer five

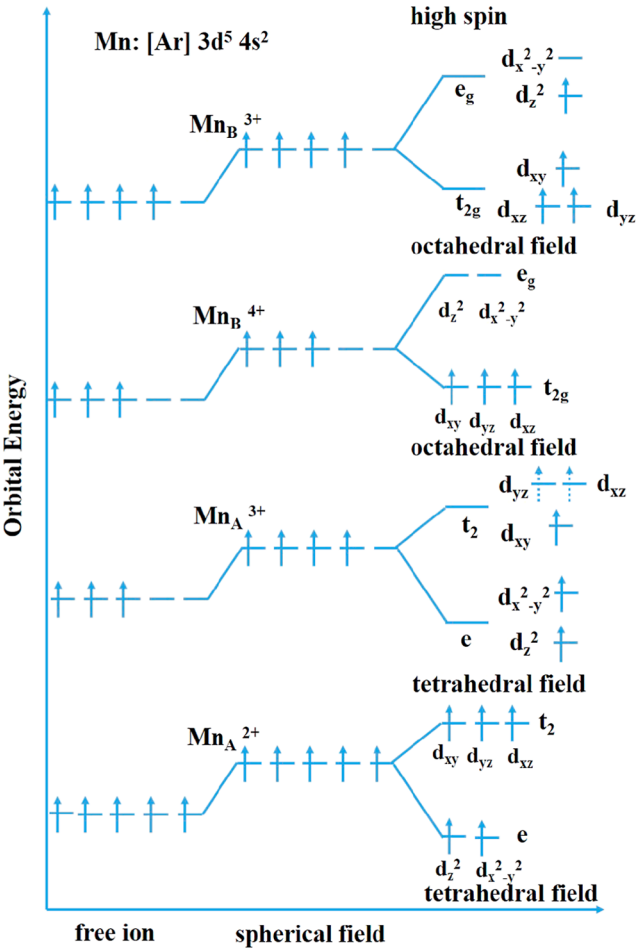

Figure 3. Graph of the crystal field splitting for the Mn 3d electrons in high-spin tetrahedral and octahedral coordination environments with the degrees of inversion $X = 0$, 0.5, and 1. The perturbation of the Mn 3d electrons in a spherical field is also represented.

electrons are half full, which means that all the degenerated orbitals are equally occupied and no JTD occurs. Moreover, it has been shown experimentally that Mn_A^{2+} in the tetrahedral site after inversion suppresses the JTD.[45,46] However, the presence of Mn_A^{2+} leads to acceleration of the dissolution of Mn ions. The Mn_A^{2+} could dissolve in the electrolyte, diffuse to the surface of the negative electrode through the electrolyte, and then undergo reduction reactions to produce metallic Mn or compounds of Mn. It destroys the solid electrolyte interface[47−49] in the negative electrode, which leads to the loss of active Li^+ and induces battery capacity decay. Mn_B^{4+} located at the octahedral field is also at a high spin state, with a fully occupied t_{2g} orbital and an empty e_g orbital. The equally occupied degenerate orbitals will not induce JTD. However, for Mn^{3+} ions with four outer electrons, there is unequal occupation of degenerate orbitals in both octahedral and tetrahedral fields. The Mn_B^{3+} 3d states in the non-distorted octahedral field are split into threefold degenerate t_{2g} orbitals (lower energy) and twofold degenerate e_g orbitals (higher energy). Three of the outer four electrons of Mn_B^{3+} at high spin states occupy the three t_{2g} orbitals, and the fourth electron occupying one of the e_g orbitals will induce unequally occupation. JTD along the c-axis will remove the degeneracy involving z-orbitals. The bond elongation along the c-axis lowers the energy of d_{z^2}, d_{xz}, and d_{yz} orbitals. As a result, the

https://doi.org/10.1021/acs.jpcc.2c00274
J. Phys. Chem. C 2022, 126, 7374−7382

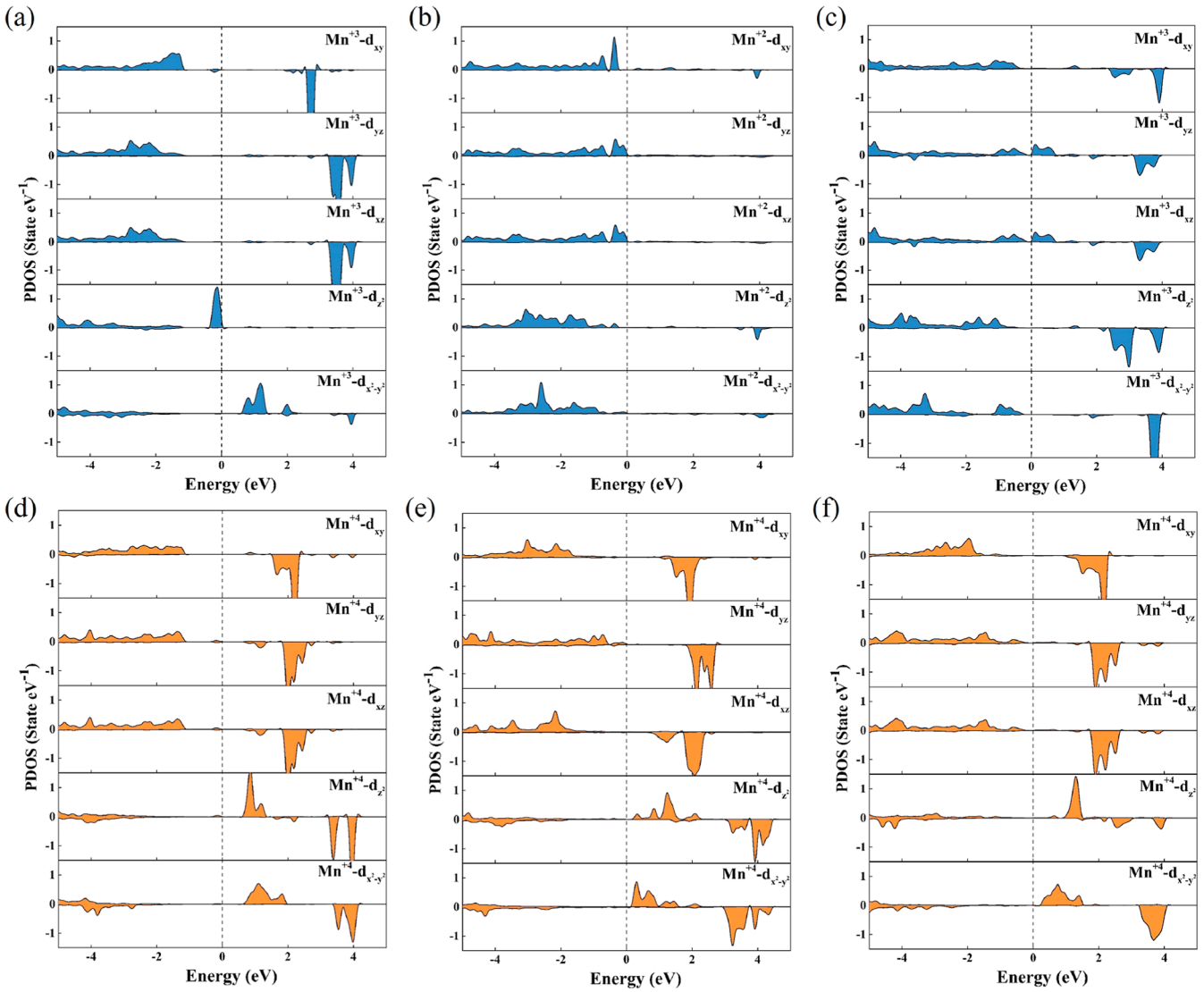

Figure 4. Higher magnetic moment Mn 3d project density of states in the (a) normal, (b) half-inverse, and (c) full-inverse LMO spinel. Lower magnetic moment Mn 3d project density of states in the (d) normal, (e) half-inverse, and (f) full-inverse LMO spinels.

four outer electrons occupy the t_{2g} and d_{z^2} orbitals, and the total energy of the system lowers. For the Mn_A^{3+} at the tetrahedral field, two of the outer electrons occupy the e orbitals and the other two electrons will introduce unequally occupied t_2 orbitals at the non-distorted structure. JTD breaks the degeneracy, and the extension along the *c*-axis will result in the electrons occupying the d_{z^2}, $d_{x^2-y^2}$, and d_{xy} orbitals and partially occupying the d_{yz} and d_{xz} orbitals as shown in Figure 3.

Our theory about the relationship of valence state, the inverse degree, the occupying site of Mn ions and the JTD could explain the experimental results. From the discussion above, the appearance of Mn^{3+} is the immediate cause of JTD. As shown in the introduction, JTD will induce the battery capacity decay. For normal and full-inverse LMO, the existence of Mn^{3+} induces large JTD and hence affects the lithium-ion battery capacity. For half-inverse LMO, the structure becomes cubic-like due to the absence of Mn^{3+}. Experimentally, the battery capacity doubles when a part of the Mn ions occupies tetrahedral sites by suppressing JTD.[7,11,46] From this perspective, an intermediate inverse degree will benefit the battery capacity. On the other hand, the appearance of Mn^{2+} ions at a half-inverse degree could exacerbate manganese dissolution and induce battery capacity decay. In all, for the stoichiometric LMO, JTD (relating to Mn^{3+}) and manganese dissolution (relating to Mn^{2+}) compete with each other with varying degrees of inversion. From the above analysis of JTD and manganese dissolution on the battery capacity, we can conclude that Mn^{2+} and Mn^{3+} ions could be considered as negative effects, while Mn^{4+} ions are always positive effects on the battery capacity. Therefore, we can use doping or substitution to increase the valence states of Mn, as has been adopted experimentally in some literature.[50,51]

Projected Density of States. To verify the crystal field theory prediction and the JTD-induced orbital splitting, the PDOSs of Mn ions with different degrees of inversion are drawn. Notably, all the Mn ions are at a high spin state, and there is no essential difference for Mn at a spin-up or a spin-down state regardless of the inverse degree, so only the results of Mn ions at the spin-up are shown.

The Mn_B 3d states in the normal LMO spinel are split into the twofold degenerate e_g orbitals and threefold degenerate t_{2g} orbitals in non-distorted octahedral fields. As discussed above, the Mn_B atoms exhibit charge separation.[23] Notice that Mn_B^{4+}

https://doi.org/10.1021/acs.jpcc.2c00274
J. Phys. Chem. C 2022, 126, 7374−7382

(lower magnetic moment) -e_g orbitals are completely unoccupied, and the energy of occupied Mn_B $3d_{xy}$, Mn_B $3d_{yz}$, and Mn_B $3d_{xz}$ is almost the same as shown in Figure 4d. This result is consistent with the crystal field prediction in Figure 3, indicating no JTD. However, for Mn_B^{3+} (higher magnetic moment) atoms, besides t_{2g} orbitals, the $3d_{z^2}$ orbital is also occupied in the spin-up channel, and the other e_g orbital ($3d_{x^2-y^2}$) with higher energy remains unoccupied as displayed in Figure 4a. The degeneracy removing of e_g orbitals indicates a distortion of the structure, and the lower energy of Mn_B^{3+} $3d_{z^2}$ means an elongation along the *c*-axis, which is consistent with the lattice constants ($c/a > 1$), the bond analysis (Figure 2), and the crystal field prediction (Figure 3). Furthermore, the energy levels of the occupied Mn_B^{3+} $3d_{xy}$ orbital in the spin-up channel are higher than energies of Mn_B^{3+} $3d_{yz}$ and Mn_B^{3+} $3d_{xz}$ orbitals that are nearly degenerate in energy, also indicating the stretching of the *c*-axis induced orbital splitting. According to crystal field theory sketched in Figure 3, JTD lowers the system energy by stretching the Mn_B^{3+}−O octahedron along the *c*-axis direction, which induces a weaker Coulomb repulsion between the O atom and Mn atom involving $3d_{z^2}$, $3d_{xz}$, and $3d_{yz}$ orbitals. The lower energies of $3d_{z^2}$, $3d_{xz}$, and $3d_{yz}$ orbitals from crystal field theory are in line with the PDOS in Figure 4. This orbital occupation of Mn_B^{3+} avoids the appearance of the degenerate ground state, reduces the structural symmetry, and lowers the total energy of the system.[42]

To gain insights into the occupation state of Mn 3d in the half-inverse LMO spinel, the PDOSs of the Mn 3d orbitals are depicted in Figure 4b,e (type I) and Figure S5 (type II to type V). The Mn_B^{4+} atoms remain at the same orbital energy level occupations as the normal spinel without obvious orbital splitting. For Mn_A^{2+} (higher magnetic moment), all the five 3d orbitals are occupied in the spin-up channel, indicating a high spin state. The energy of degenerate e orbitals is lower than that of t_2 orbitals, which is consistent with crystal field prediction in Figure 3.

There is an interesting phenomenon that strong JTD is observed in the Mn_A^{3+}−O tetrahedron when the LMO spinel fully inverses. The occupation state of Mn 3d in the full-inverse LMO spinel is illustrated in Figure 4c,f (type I) and Figure S10 (type II and type III). On the one hand, the Mn_B^{4+} atom remains at the same orbital energy level occupation since it is still at the octahedral field as shown in Figure 3 for the non-distorted Mn_B^{4+}−O octahedron from crystal field theory prediction. On the other hand, the energies of Mn_A^{3+} t_2 orbitals and Mn_A^{3+} e orbitals are both split. The energy of the occupied Mn_A^{3+} $3d_{z^2}$ orbital is lower than that of the other e orbital Mn_A^{3+} $3d_{x^2-y^2}$, indicating an elongation of the tetrahedra along the *c*-axis. The Mn_A^{3+} $3d_{xy}$ orbital occupies the spin-up channels, while the Mn_A^{3+} $3d_{yz}$ and Mn_A^{3+} $3d_{xz}$ orbitals which are nearly degenerate in energy partially occupy the spin-up channels as shown in Figure 4c. The elongation of the Mn_A^{3+}−O tetrahedron along the *c*-axis direction increases the distance between the Mn_A^{3+} $3d_{xy}$ orbital and the ligand O atoms, so the Coulomb repulsion between them decreases and the orbital energy level goes down. At the same time, the distance between the Mn_A^{3+} $3d_{yz}$ (Mn_A^{3+} $3d_{xz}$) orbital and O orbital decreases, resulting in a rise in their energy levels.

CONCLUSIONS

We studied the structures and the electronic occupation of LMO spinels with different degrees of inversion. The results show that inversion plays a conflicting role in the capacity decay of lithium-ion batteries. As discussed, Mn^{3+} is related to the JTD, and Mn^{2+} is related to the dissolution of Mn, both of which deteriorate the battery capacity. The Mn^{4+} ions occupied the octahedral sites, for all the inversion degrees are positive effects on the battery capacity. The inversion changes their charge values and ordering. For the normal and full-inverse spinel, Mn^{3+} ions occupy octahedral sites and tetrahedral sites, respectively. The possible unequal occupations at the degenerated energy levels of Mn^{3+} ions induce strong JTD, which will disrupt the three-dimensional channels of lithium ions and reduce the battery capacity. For the half-inverse spinel, the tetrahedral sites are occupied by Mn^{2+}, inducing cubic-like structures. Even though the JTD is suppressed due to the vanishing of Mn^{3+}, the existence of Mn^{2+} speeds up the dissolution of manganese which also degenerates the battery capacity. In conclusion, inversion in orthorhombic LMO spinels does not always negatively affect the cell capacity as JTD and dissolution of Mn^{2+} compete with each other. Furthermore, for all the three degrees of inversion studied, the manganese ions remain in high spin states, and there is a law that the lower the valence state of manganese ions, the higher the spin magnetic moments: $q(Mn^{2+}) < q(Mn^{3+}) < q(Mn^{4+})$, $m_s(Mn^{4+}) < m_s(Mn^{3+}) < m_s(Mn^{2+})$.

ASSOCIATED CONTENT

Supporting Information

The Supporting Information is available free of charge at https://pubs.acs.org/doi/10.1021/acs.jpcc.2c00274.

Energies, charge values, magnetic moments, JTD, and projected density of state (PDOS) of the other possible structures at inverse degrees $X = 0.5$ and $X = 1.0$ (PDF)

AUTHOR INFORMATION

Corresponding Author

Dongwei Xu − *State Key Laboratory of Coal Combustion, School of Energy and Power Engineering, Huazhong University of Science and Technology, Wuhan, Hubei 430074, China;* orcid.org/0000-0002-5847-3711; Email: dwxu@hust.edu.cn

Authors

Zijing Wan − *State Key Laboratory of Coal Combustion, School of Energy and Power Engineering, Huazhong University of Science and Technology, Wuhan, Hubei 430074, China*

Yaxin Xu − *State Key Laboratory of Coal Combustion, School of Energy and Power Engineering, Huazhong University of Science and Technology, Wuhan, Hubei 430074, China*

Guoqing Sun − *State Key Laboratory of Coal Combustion, School of Energy and Power Engineering, Huazhong University of Science and Technology, Wuhan, Hubei 430074, China*

Xiaobing Luo − *State Key Laboratory of Coal Combustion, School of Energy and Power Engineering, Huazhong University of Science and Technology, Wuhan, Hubei 430074, China;* orcid.org/0000-0002-6423-9868

Complete contact information is available at: https://pubs.acs.org/10.1021/acs.jpcc.2c00274

Notes

The authors declare no competing financial interest.

https://doi.org/10.1021/acs.jpcc.2c00274
J. Phys. Chem. C 2022, 126, 7374−7382

■ ACKNOWLEDGMENTS

D.X. acknowledges support from the National Natural Science Foundation of China (No. 51806072). Some of the computation was completed using the Tianhe II supercomputer in the National Super-computing Center at Guangzhou.

■ REFERENCES

(1) He, X.; Wang, J.; Kloepsch, R.; Krueger, S.; Jia, H.; Liu, H.; Vortmann, B.; Li, J. Enhanced electrochemical performance in lithium ion batteries of a hollow spherical lithium-rich cathode material synthesized by a molten salt method. *Nano Res.* **2014**, *7*, 110−118.

(2) Zeng, X.; Li, M.; Abd El-Hady, D.; Alshitari, W.; Al-Bogami, A. S.; Lu, J.; Amine, K. Commercialization of lithium battery technologies for electric vehicles. *Adv. Energy Mater.* **2019**, *9*, 1900161.

(3) Xi, L. J.; Wang, H.-E.; Lu, Z. G.; Yang, S. L.; Ma, R. G.; Deng, J. Q.; Chung, C. Y. Facile synthesis of porous $LiMn_2O_4$ spheres as positive electrode for high-power lithium ion batteries. *J. Power Sources* **2012**, *198*, 251−257.

(4) Gummow, R. J.; Liles, D.; Thackeray, M. Lithium extraction from orthorhombic lithium manganese oxide and the phase transformation to spinel. *Mater. Res. Bull.* **1993**, *28*, 1249−1256.

(5) David, W. I. F.; Thackeray, M. M.; Bruce, P. G.; Goodenough, J. B. Lithium insertion into β-MnO_2 and the rutile-spinel transformation. *Mater. Res. Bull.* **1984**, *19*, 99−106.

(6) Kugel', K. I.; Khomskiĭ, D. I. The Jahn-Teller effect and magnetism: transition metal compounds. *Sov. Phys. Usp.* **1982**, *25*, 231.

(7) Zuo, C.; Hu, Z.; Qi, R.; Liu, J.; Li, Z.; Lu, J.; Dong, C.; Yang, K.; Huang, W.; Chen, C.; et al. Double the Capacity of Manganese Spinel for Lithium-Ion Storage by Suppression of Cooperative Jahn−Teller Distortion. *Adv. Eng. Mater.* **2020**, *10*, 2000363.

(8) Leung, K. First-Principles Modeling of Mn (II) Migration above and Dissolution from $Li_xMn_2O_4$ (001) Surfaces. *Chem. Mater.* **2017**, *29*, 2550−2562.

(9) Zheng, H.; Sun, Q.; Liu, G.; Song, X.; Battaglia, V. S. Correlation between dissolution behavior and electrochemical cycling performance for $LiNi_{1/3}Co_{1/3}Mn_{1/3}O_2$ -based cells. *J. Power Sources* **2012**, *207*, 134−140.

(10) Thackeray, M. M.; Johnson, P. J.; De Picciotto, L. A.; Bruce, P. G.; Goodenough, J. B. Electrochemical extraction of lithium from $LiMn_2O_4$. *Mater. Res. Bull.* **1984**, *19*, 179−187.

(11) Rodríguez, R. A.; Mohallem, N. D. S.; Santos, M. A.; Costa, D. A. S.; Montoro, L. A.; Laffita, Y. M.; Carrasco, L. A. T.; Perez-Cappe, E. L. Unveiling the role of Mn-interstitial defect and particle size on the Jahn-Teller distortion of the $LiMn_2O_4$ cathode material. *J. Power Sources* **2021**, *490*, 229519.

(12) Anderson, P. W. Ordering and antiferromagnetism in ferrites. *Phys. Rev.* **1956**, *102*, 1008.

(13) Gao, A.; Hou, X.; Sun, Z.; Li, S.; Li, H.; Zhang, J. Lithium-desorption mechanism in $LiMn_2O_4$, $Li_{1.33}Mn_{1.67}O_4$, and $Li_{1.6}Mn_{1.6}O_4$ according to precisely controlled acid treatment and density functional theory calculations. *J. Mater. Chem. A* **2019**, *7*, 20878−20890.

(14) Chinnasamy, C. N.; Narayanasamy, A.; Ponpandian, N.; Chattopadhyay, K.; Shinoda, K.; Jeyadevan, B.; Tohji, K.; Nakatsuka, K.; Furubayashi, T.; Nakatani, I. Mixed spinel structure in nanocrystalline $NiFe_2O_4$. *Phys. Rev. B: Condens. Matter Mater. Phys.* **2001**, *63*, 184108.

(15) Santos-Carballal, D.; Roldan, A.; Grau-Crespo, R.; de Leeuw, N. H. First-principles study of the inversion thermodynamics and electronic structure of FeM_2X_4 (thio)spinels (M= Cr, Mn, Co, Ni; X= O, S). *Phys. Rev. B: Condens. Matter Mater. Phys.* **2015**, *91*, 195106.

(16) Wu, G.; Wang, J.; Ding, W.; Nie, Y.; Li, L.; Qi, X.; Chen, S.; Wei, Z. A strategy to promote the electrocatalytic activity of spinels for oxygen reduction by structure reversal. *Angew. Chem., Int. Ed.* **2016**, *55*, 1340−1344.

(17) Karim, A.; Fosse, S.; Persson, K. A. Surface structure and equilibrium particle shape of the $LiMn_2O_4$ spinel from first-principles calculations. *Phys. Rev. B: Condens. Matter Mater. Phys.* **2013**, *87*, 075322.

(18) Santos-Carballal, D.; Ngoepe, P. E.; De Leeuw, N. H. Ab initio investigation of the thermodynamics of cation distribution and of the electronic and magnetic structures in the $LiMn_2O_4$ spinel. *Phys. Rev. B* **2018**, *97*, 085126.

(19) Benedek, R.; Thackeray, M. M. Simulation of the surface structure of lithium manganese oxide spinel. *Phys. Rev. B: Condens. Matter Mater. Phys.* **2011**, *83*, 195439.

(20) Rodríguez-Carvajal, J.; Rousse, G.; Masquelier, C.; Hervieu, M. Electronic crystallization in a lithium battery material: columnar ordering of electrons and holes in the spinel $LiMn_2O_4$. *Phys. Rev. Lett.* **1998**, *81*, 4660.

(21) Ishizawa, N.; Tateishi, K.; Oishi, S.; Kishimoto, S. Bond-length fluctuation in the orthorhombic 3× 3× 1 superstructure of $LiMn_2O_4$ spinel. *Am. Mineral.* **2014**, *99*, 1528−1536.

(22) Tomeno, I.; Kasuya, Y.; Tsunoda, Y. Charge and spin ordering in $LiMn_2O_4$. *Phys. Rev. B: Condens. Matter Mater. Phys.* **2001**, *64*, 094422.

(23) Ouyang, C. Y.; Shi, S. Q.; Lei, M. S. Jahn−Teller distortion and electronic structure of $LiMn_2O_4$. *J. Alloys Compd.* **2009**, *474*, 370−374.

(24) Jaber-Ansari, L.; Puntambekar, K. P.; Kim, S.; Aykol, M.; Luo, L.; Wu, J.; Myers, B. D.; Iddir, H.; Russell, J. T.; Saldaña, S. J.; et al. Suppressing manganese dissolution from lithium manganese oxide spinel cathodes with single-layer graphene. *Adv. Energy Mater.* **2015**, *5*, 1500646.

(25) Scivetti, I.; Teobaldi, G. (Sub) surface-promoted disproportionation and absolute band alignment in high-power $LiMn_2O_4$ cathodes. *J. Phys. Chem. C* **2015**, *119*, 21358−21368.

(26) Wills, A. S.; Raju, N. P.; Greedan, J. E. Low-temperature structure and magnetic properties of the spinel $LiMn_2O_4$: a frustrated antiferromagnet and cathode material. *Chem. Mater.* **1999**, *11*, 1510−1518.

(27) Chukalkin, Y. G.; Teplykh, A. E.; Pirogov, A. N.; Kellerman, D. G. Magnetism of $LiMn_2O_4$ manganite in structurally ordered and disordered states. *Phys. Solid State* **2010**, *52*, 2545−2551.

(28) Liu, W.-W.; Wang, D.; Wang, Z.; Deng, J.; Lau, W.-M.; Zhang, Y. Influence of magnetic ordering and Jahn−Teller distortion on the lithiation process of $LiMn_2O_4$. *Phys. Chem. Chem. Phys.* **2017**, *19*, 6481−6486.

(29) Kresse, G.; Furthmüller, J.; Hafner, J. Theory of the crystal structures of selenium and tellurium: the effect of generalized-gradient corrections to the local-density approximation. *Phys. Rev. B: Condens. Matter Mater. Phys.* **1994**, *50*, 13181.

(30) Kresse, G.; Furthmüller, J. Efficient iterative schemes for ab initio total-energy calculations using a plane-wave basis set. *Phys. Rev. B: Condens. Matter Mater. Phys.* **1996**, *54*, 11169.

(31) Kresse, G.; Joubert, D. From ultrasoft pseudopotentials to the projector augmented-wave method. *Phys. Rev. B: Condens. Matter Mater. Phys.* **1999**, *59*, 1758.

(32) Perdew, J. P.; Burke, K.; Ernzerhof, M. Generalized gradient approximation made simple. *Phys. Rev. Lett.* **1996**, *77*, 3865.

(33) Tang, D.; Sun, Y.; Yang, Z.; Ben, L.; Gu, L.; Huang, X. Surface structure evolution of $LiMn_2O_4$ cathode material upon charge/discharge. *Chem. Mater.* **2014**, *26*, 3535−3543.

(34) Dudarev, S. L.; Botton, G. A.; Savrasov, S. Y.; Humphreys, C. J.; Sutton, A. P. Electron-energy-loss spectra and the structural stability of nickel oxide: An LSDA+ U study. *Phys. Rev. B: Condens. Matter Mater. Phys.* **1998**, *57*, 1505.

(35) Xu, B.; Qian, D.; Wang, Z.; Meng, Y. S. Recent progress in cathode materials research for advanced lithium ion batteries. *Mater. Sci. Eng. R Rep.* **2012**, *73*, 51−65.

(36) Peles, A. GGA+ U method from first principles: application to reduction−oxidation properties in ceria-based oxides. *J. Mater. Sci.* **2012**, *47*, 7542−7548.

https://doi.org/10.1021/acs.jpcc.2c00274
J. Phys. Chem. C 2022, 126, 7374−7382

(37) Tolba, S. A.; Gameel, K. M.; Ali, B. A.; Almossalami, H. A.; Allam, N. K. In *Density Functional Calculations*; Yang, G., Ed.; IntechOpen: Rijeka, 2018; Chapter 1.
(38) Tang, W.; Sanville, E.; Henkelman, G. A grid-based Bader analysis algorithm without lattice bias. *J. Phys. Condens. Matter* **2009**, *21*, 084204.
(39) Roldan, A.; Santos-Carballal, D.; de Leeuw, N. H. A comparative DFT study of the mechanical and electronic properties of greigite Fe_3S_4 and magnetite Fe_3O_4. *J. Chem. Phys.* **2013**, *138*, 204712.
(40) Toyama, T.; Hirano, T.; Okumura, T.; Horiba, T. X-ray absorption fine structure analysis for crystal structure change of vanadium-substituted lithium silicate, $Li_{2.2}Fe_{0.4}Mn_{0.4}Si_{0.8}V_{0.2}O_4$, during charge-discharge cycles. *J. Power Sources* **2019**, *443*, 227189.
(41) Deng, W.; Li, Z.; Ye, Y.; Zhou, Z.; Li, Y.; Zhang, M.; Yuan, X.; Hu, J.; Zhao, W.; Huang, Z.; et al. Zn^{2+} Induced Phase Transformation of K_2MnFe (CN) 6 Boosts Highly Stable Zinc-Ion Storage. *Adv. Eng. Mater.* **2021**, *11*, 2003639.
(42) Liu, Z.; Pan, J.; Zhang, Y.-F.; Du, S. Half-auxetic effect and ferroelasticity in a two-dimensional monolayer TiSe. *J. Phys. Condens. Matter* **2021**, *33*, 144002.
(43) Baur, W. H. The geometry of polyhedral distortions. Predictive relationships for the phosphate group. *Acta Crystallogr., Sect. B: Struct. Crystallogr. Cryst. Chem.* **1974**, *30*, 1195−1215.
(44) Yang, H.; Savory, C. N.; Morgan, B. J.; Scanlon, D. O.; Skelton, J. M.; Walsh, A. Chemical Trends in the Lattice Thermal Conductivity of Li(Ni, Mn, Co)O_2 (NMC) Battery Cathodes. *Chem. Mater.* **2020**, *32*, 7542−7550.
(45) Antao, S. M.; Cruickshank, L. A.; Hazrah, K. S. Structural trends and solid-solutions based on the crystal chemistry of two hausmannite (Mn_3O_4) samples from the kalahari manganese field. *Minerals* **2019**, *9*, 343.
(46) Rodríguez, R. A.; Montiel, M. G.; Mohallem, N. D. S.; Laffita, Y. M.; Montoro, L. A.; Santos, M. A.; Ramírez, H. L.; Pérez-Cappe, E. L. The role of defects on the Jahn-teller effect and electrochemical charge storage in nanometric $LiMn_2O_4$ material. *Solid State Ionics* **2021**, *369*, 115707.
(47) Wang, A.; Kadam, S.; Li, H.; Shi, S.; Qi, Y. Review on modeling of the anode solid electrolyte interphase (SEI) for lithium-ion batteries. *npj Comput. Mater.* **2018**, *4*, 15.
(48) Soto, F. A.; Marzouk, A.; El-Mellouhi, F.; Balbuena, P. B. Understanding ionic diffusion through SEI components for lithium-ion and sodium-ion batteries: insights from first-principles calculations. *Chem. Mater.* **2018**, *30*, 3315−3322.
(49) Aupperle, F.; von Aspern, N.; Berghus, D.; Weber, F.; Eshetu, G. G.; Winter, M.; Figgemeier, E. The role of electrolyte additives on the interfacial chemistry and thermal reactivity of Si-anode-based Li-ion battery. *ACS Appl. Energy Mater.* **2019**, *2*, 6513−6527.
(50) Zhang, W.; Sun, X.; Tang, Y.; Xia, H.; Zeng, Y.; Qiao, L.; Zhu, Z.; Lv, Z.; Zhang, Y.; Ge, X.; et al. Lowering charge transfer barrier of $LiMn_2O_4$ via nickel surface doping to enhance Li+ intercalation kinetics at subzero temperatures. *J. Am. Chem. Soc.* **2019**, *141*, 14038−14042.
(51) Zhang, S.; Deng, W.; Momen, R.; Yin, S.; Chen, J.; Massoudi, A.; Zou, G.; Hou, H.; Deng, W.; Ji, X. Element substitution of a spinel $LiMn_2O_4$ cathode. *J. Mater. Chem. A* **2021**, *9*, 21532−21550.

https://doi.org/10.1021/acs.jpcc.2c00274
J. Phys. Chem. C 2022, 126, 7374−7382